Supplementary information for

Atomic-scale quantification of individual oxygen vacancies and structural evolution in valence change memristors

Zhengzhou Wang[1,2]†, Weixiao Lin[1,2]†, Yongqiang Li[1,2], Meiyan Wang[1,2], Anan Guo[1,2], Hao Luo[1,2], Xiahan Sang[1,2], Lei Jin[3], Cheng Chen[1], Wen Zhao[4], Heguang Liu[5], Rafal E. Dunin-Borkowski[3]*, Jinsong Wu[1,2,6]*

[1]*State Key Laboratory of Advanced Technology for Materials Synthesis and Processing, Wuhan University of Technology, Wuhan 430070, China.*

[2]*Hubei Longzhong Laboratory, Wuhan University of Technology (Xiangyang Demonstration Zone), Xiangyang 441000, Hubei, China.*

[3]*Ernst Ruska-Centre for Microscopy and Spectroscopy with Electrons (ER-C), Forschungszentrum Jülich GmbH, 52425 Jülich, Germany*

[4]*School of Materials Science and Engineering, China University of Petroleum (East China), Qingdao 266580, China*

[5]*School of Materials Science and Engineering, Xi'an University of Technology, Xi'an 710048, China*

[6]*Yangtze Laboratory, Wuhan 430205, China*

*Correspondence and requests for materials should be addressed to Rafal E. Dunin-Borkowski and Jinsong Wu (r.dunin-borkowski@fz-juelich.de, wujs@whut.edu.cn)

†These authors contributed equally to this work

Additional experimental details including:

Supplementary Fig. 1−30, Supplementary Table 1 and Supplementary Movie 1

References

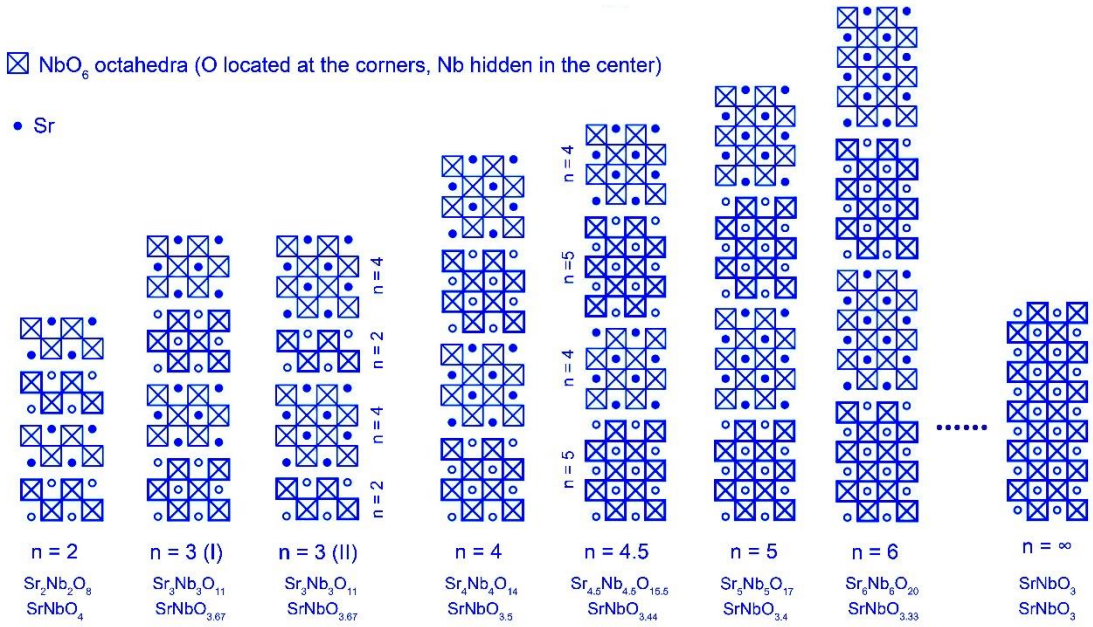

Supplementary Fig. 1. Schematic representation of the idealized crystal structures of the n = 2, 3, 4, 4.5, 5, 6 and ∞ members of the $Sr_nNb_nO_{3n+2}$ type structures.

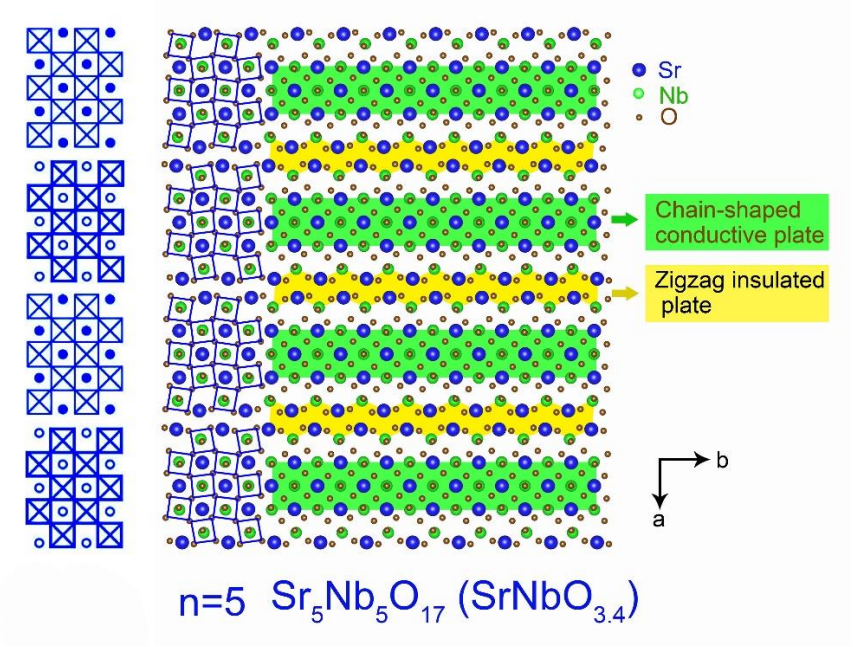

Supplementary Fig. 2. Chain-shaped conductive plates and zigzag insulating plates in the $SrNbO_{3.4}$ crystal structure.

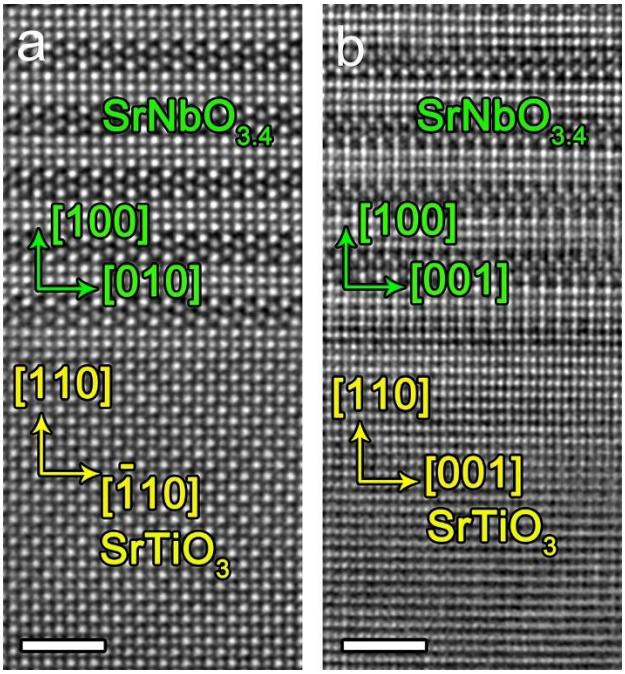

Supplementary Fig. 3. The epitaxial relationship between SNO film and NSTO substrate. Scale bar=2 nm.

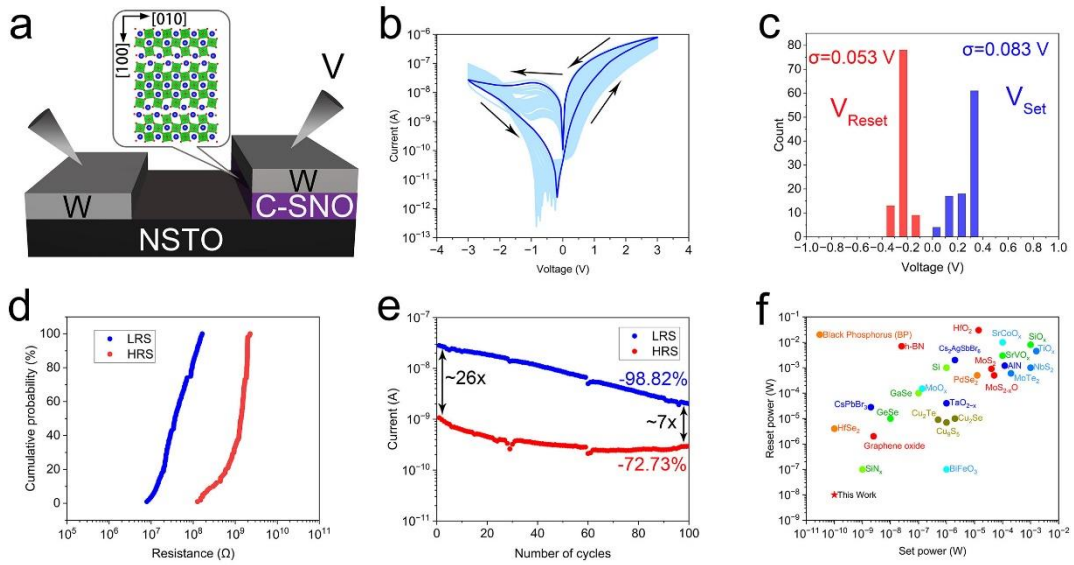

Supplementary Fig. 4. Electrical characterizations of NSTO/SNO/W memristors. **(a)** The structure schematic of the memristor. **(b)** I–V curves of a NSTO/SNO/W memristor during 100 cycles. The arrows indicate the direction of the scanning voltage. **(c)** The corresponding histogram of Set voltage and Reset voltage extracted from **b**. **(d)** The cumulative probability distribution of the resistance in HRS and LRS. The resistances are acquired from 100 cycles at 0.48 V. **(e)** The endurance characteristics of the memristor undergoing over 100 cycles. **(f)** The comparison of Set and Reset power consumption for different memristors. The pentagrams represent the NSTO/SNO/W device. The reference data are sourced from the reported bipolar memristors[1-27].

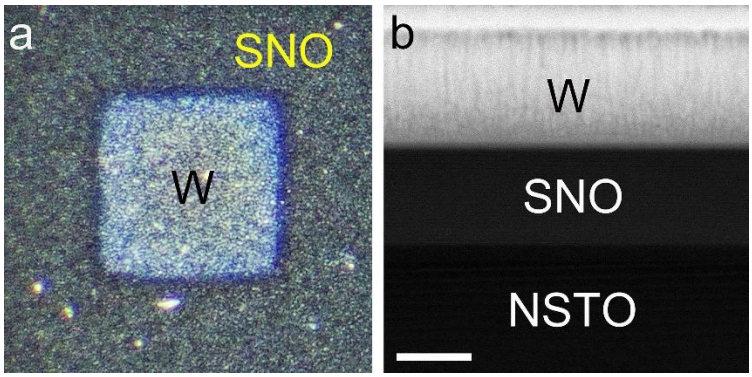

Supplementary Fig. 5. The SNO device after cycle. (a) The optical microscope image of the W electrode. **(b)** The cross-section STEM image of the device. Scale bar=50 nm.

Unlike memristors based on an electrochemical metallization mechanism (ECM), in which metal ions from an active electrode infiltrate the channel and make contact with another inert electrode to form a conductive path, SNO devices employ an inert electrode (W). In addition, after hundreds of switching operations, no significant ion accumulation was observed around the electrode and in the oxide/electrode interface (Supplementary Fig. 5). In other words, memristor behavior is the essence of SNO under voltage-induced electric field. The resistance switch feature is associated with the associated oxygen vacancy, not the metal electrode.

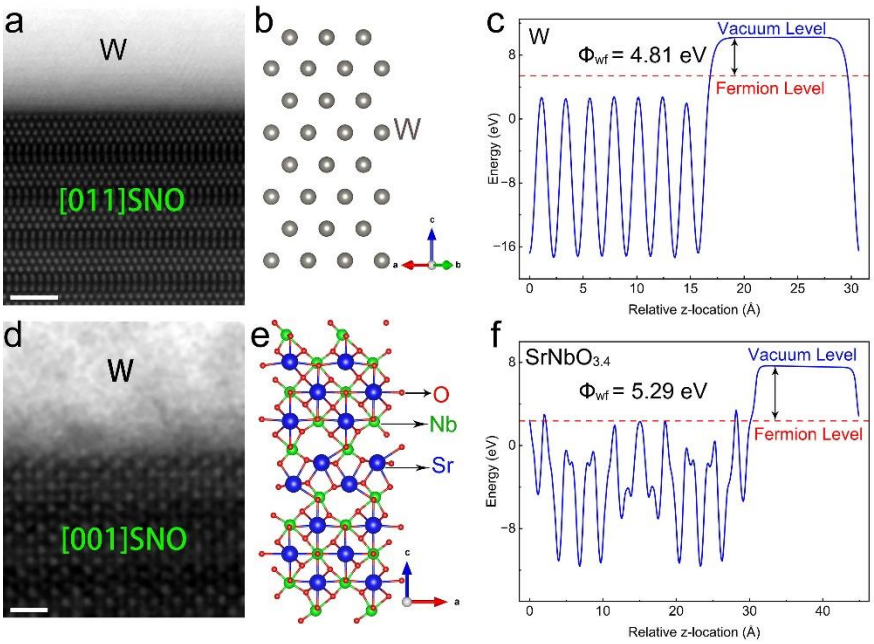

Supplementary Fig. 6. The work function of W and SNO. (a) The interface between SNO in the [011] directions and W. Scale bar=2 nm. **(b)** The atomic model in the [110] zone axis of W. **(c)** The work function of W. **(d)** The interface between SNO in the [001] directions and W. Scale bar=1 nm. **(e)** The atomic model in the [001] zone axis of SNO. **(f)** The work function of SNO.

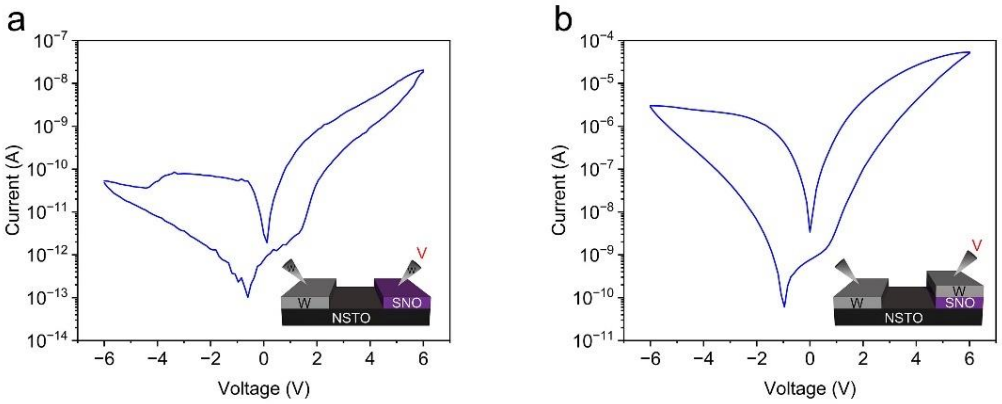

Supplementary Fig. 7. The measured I-V curve of devices with different electrode sizes (W needle: ~10^2 μm^2 and W electrode: ~9×10^4 μm^2).

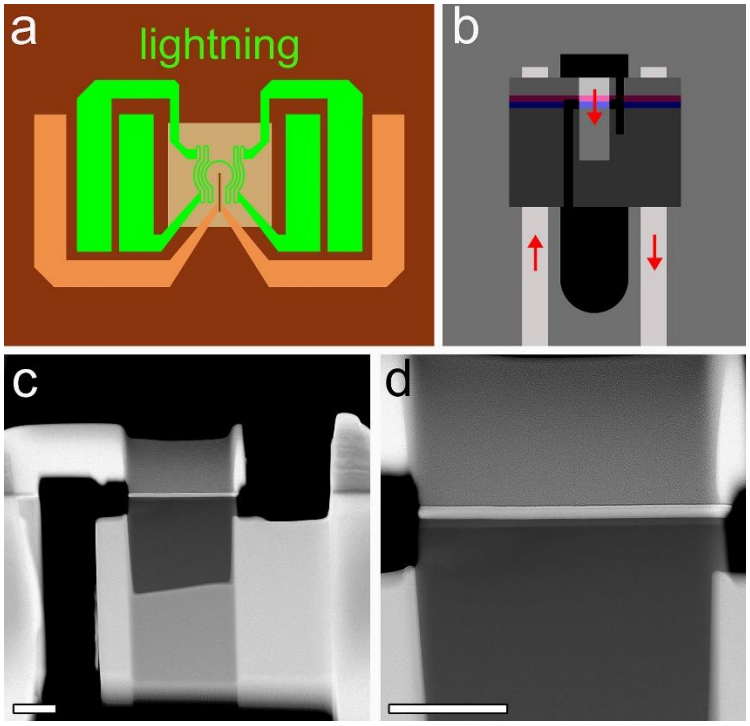

Supplementary Fig. 8. The design of *in-situ* electrical experiment. (a) The schematic illustration of the integrated biasing and heating chip. **(b)** The sample setup on the DENSsolution TEM holder. **(c**, **d)** The STEM images of the sample prepared by focused ion beam (FIB). Scale bar=1 μm.

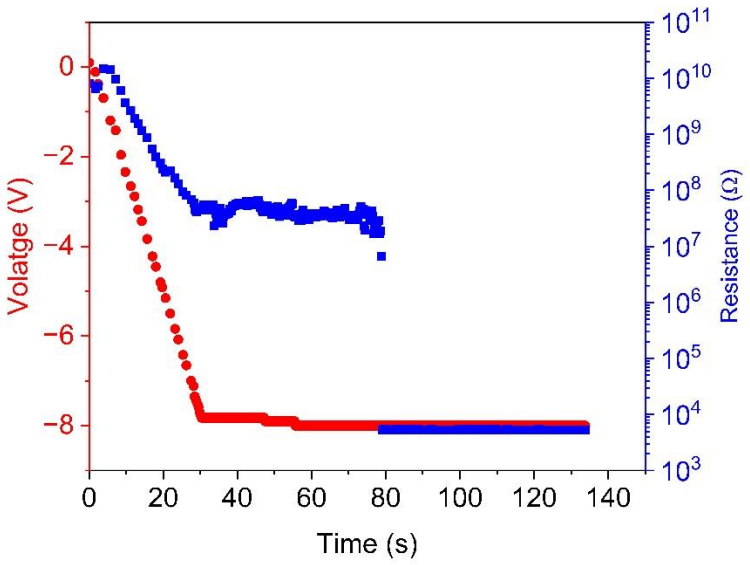

Supplementary Fig. 9. *In-situ* resistive-voltage characteristics of the NSTO/SNO/W device under applied bias.

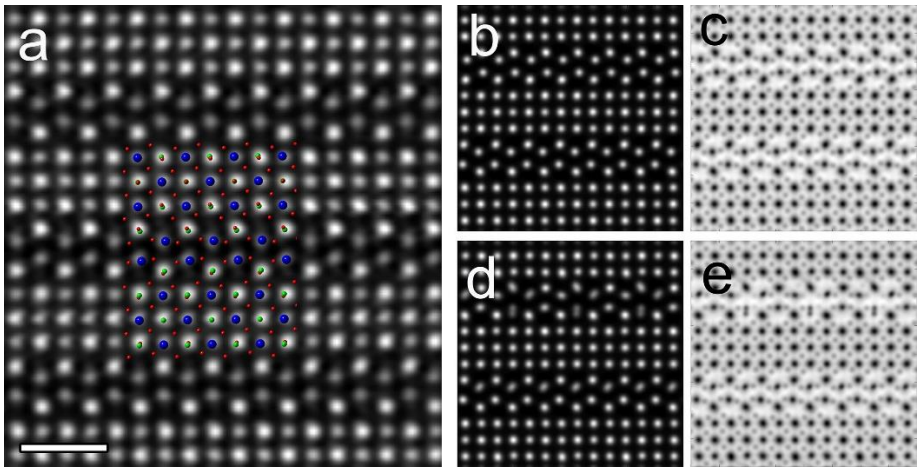

Supplementary Fig. 10. The QSTEM simulation of HAADF and ABF. (a) The HAADF image of the experiment. Scale bar=1 nm. **(b, c)** The simulated HAADF and ABF images without oxygen vacancies. **(d, e)** The simulated HAADF and ABF images containing an oxygen vacancy.

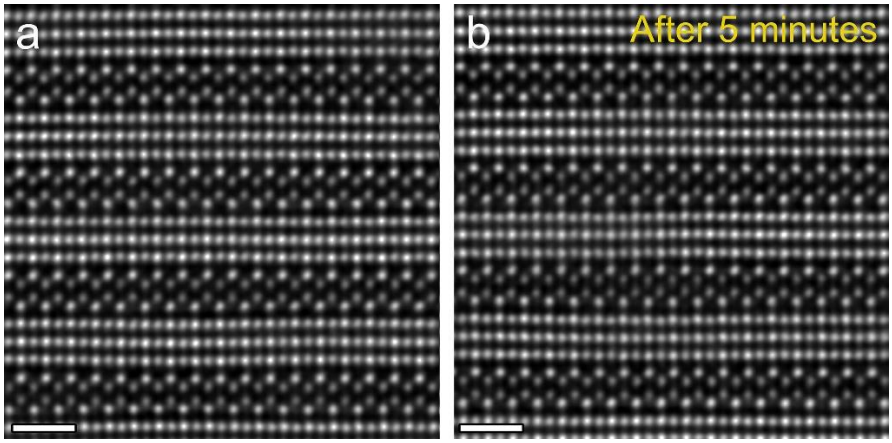

Supplementary Fig. 11. The HAADF images before (a) and after (b) the continuous 5-minute electron beam irradiation. Scale bar=1 nm.

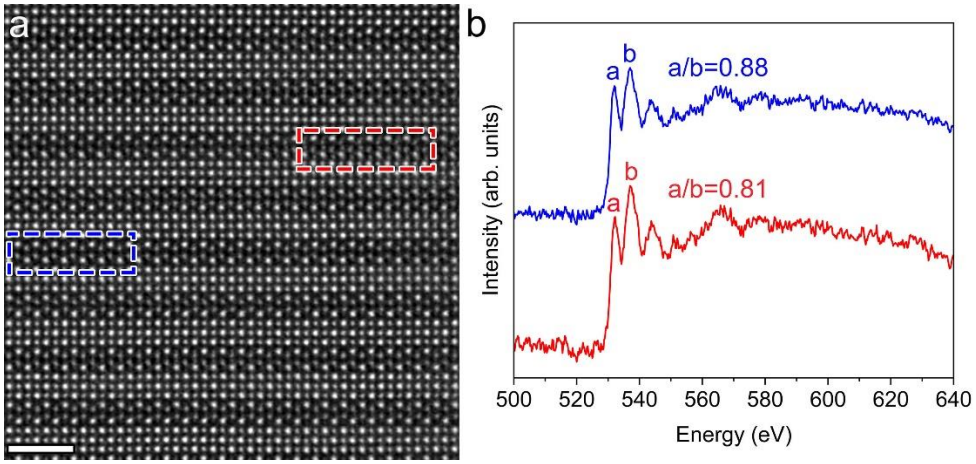

Supplementary Fig. 12. The EELS spectra of the O−K edges taken from the oxygen-rich layer of the $SrNbO_{3.4}$. (a) The high-resolution HAADF image in the [001] zone axis of SNO. Scale bar=2 nm. **(b)** The EELS spectra of the area with dotted rectangular box (oxygen-rich) in **a**.

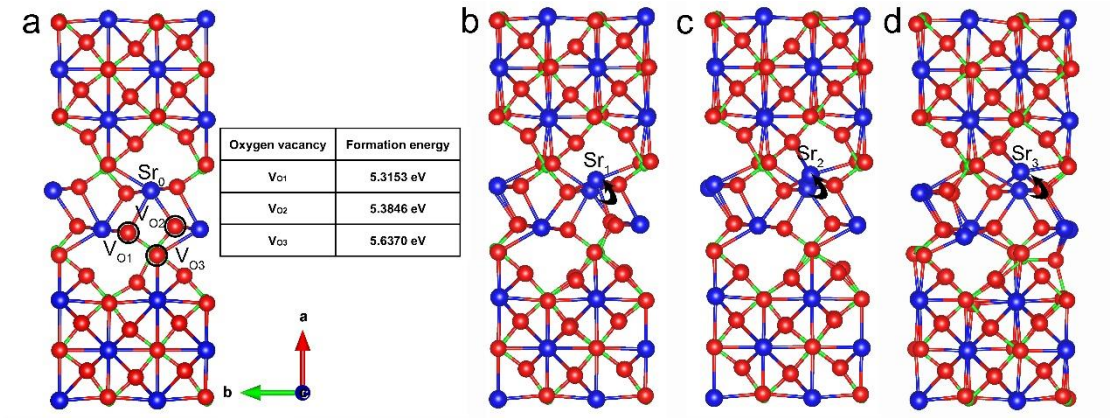

Supplementary Fig. 13. The DFT calculation of oxygen vacancy formation energy and configuration. (a) The formation energy of oxygen vacancy (oxygen atom marked with black circle). **(b-d)** The change of Sr atom position after the appearance of 1, 2 and 3 oxygen vacancies.

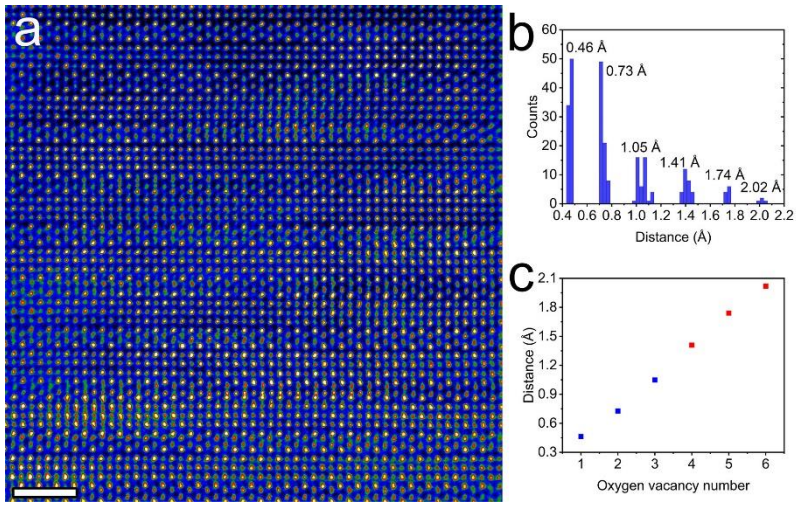

Supplementary Fig. 14. The relationship between the distance of Sr atom deviation and the concentration of oxygen vacancy. (a) The HAADF image after applying bias *in-situ*. Scale bar=2 nm. **(b)** The histogram of the statistical distribution of the deviation distance of Sr atoms in **a**. The values inserted in the graph are averages. **(c)** The scatter plot of the distance of Sr atom deviation with oxygen vacancy concentration.

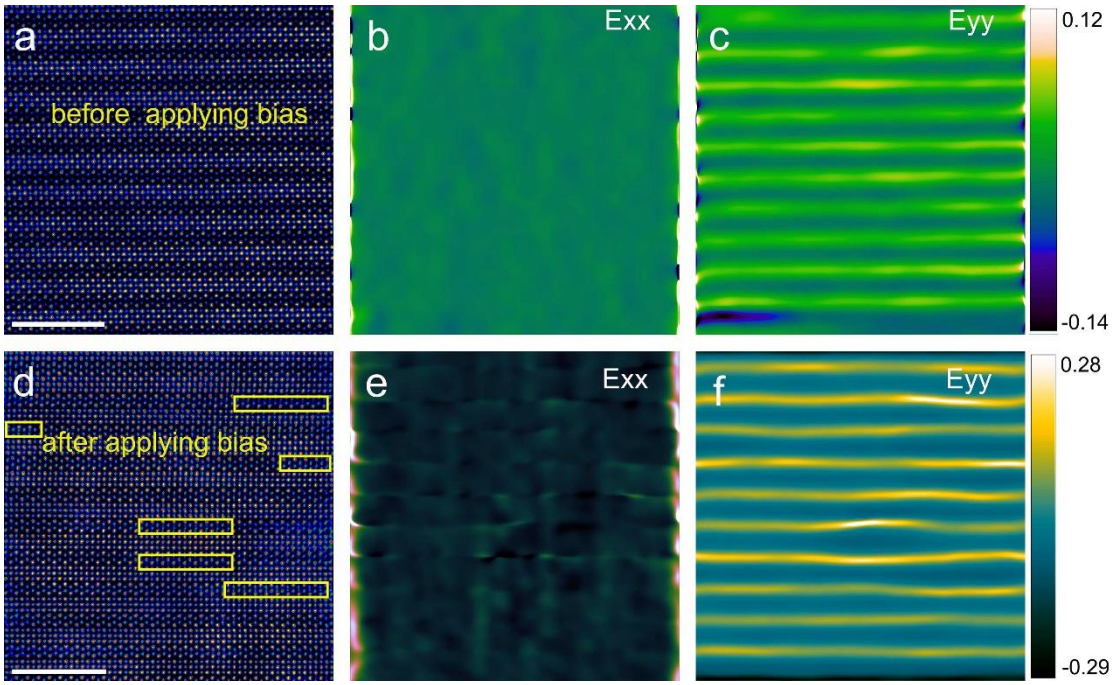

Supplementary Fig. 15. The GPA maps before and after applying the voltage (-8 V). (a) The HAADF image before applying bias. Scale bar=5 nm. **(b, c)** The GPA maps of **a**. **d**, The HAADF image after applying bias. Scale bar=5 nm. **(e, f)** The GPA maps of **d**.

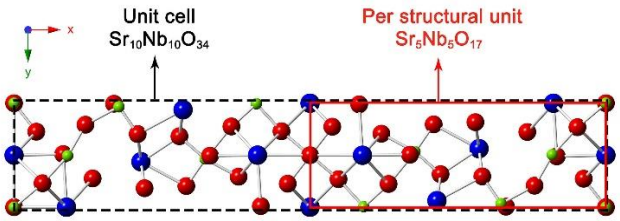

Supplementary Fig. 16. The per structural unit (a molecular formula of $Sr_5Nb_5O_{17}$, which consists of 5 Sr atoms, 5 Nb atoms and 17 oxygen atoms).

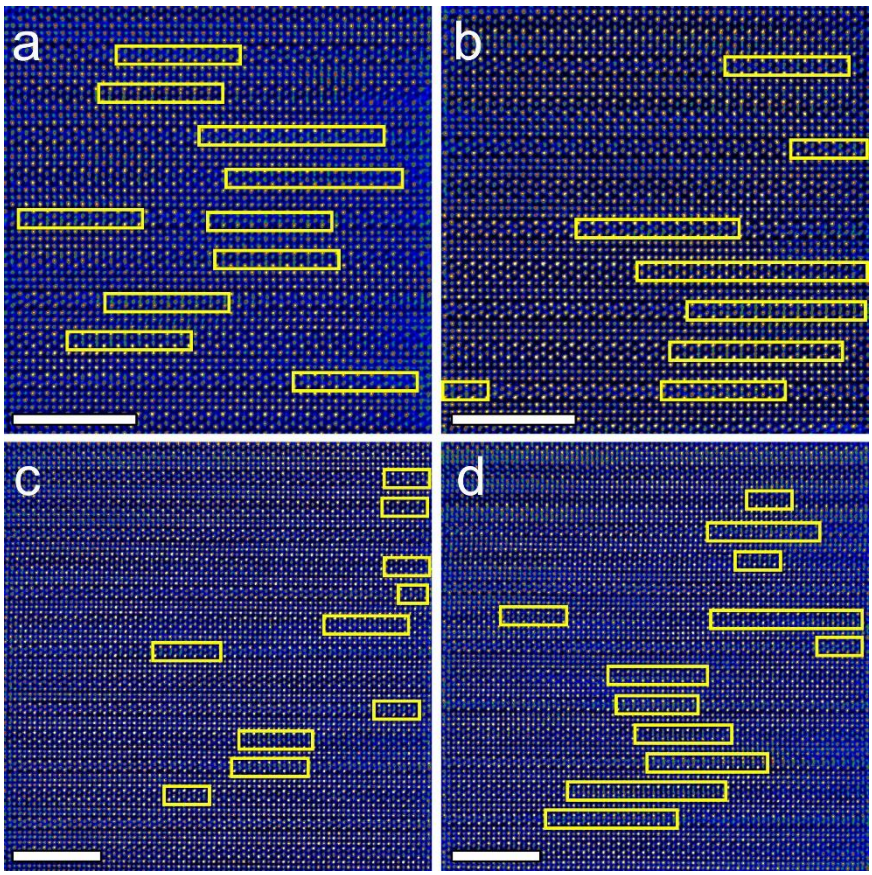

Supplementary Fig. 17. The HAADF images of NSTO/SNO/W after *in-situ* applying bias. Scale bar=5 nm.

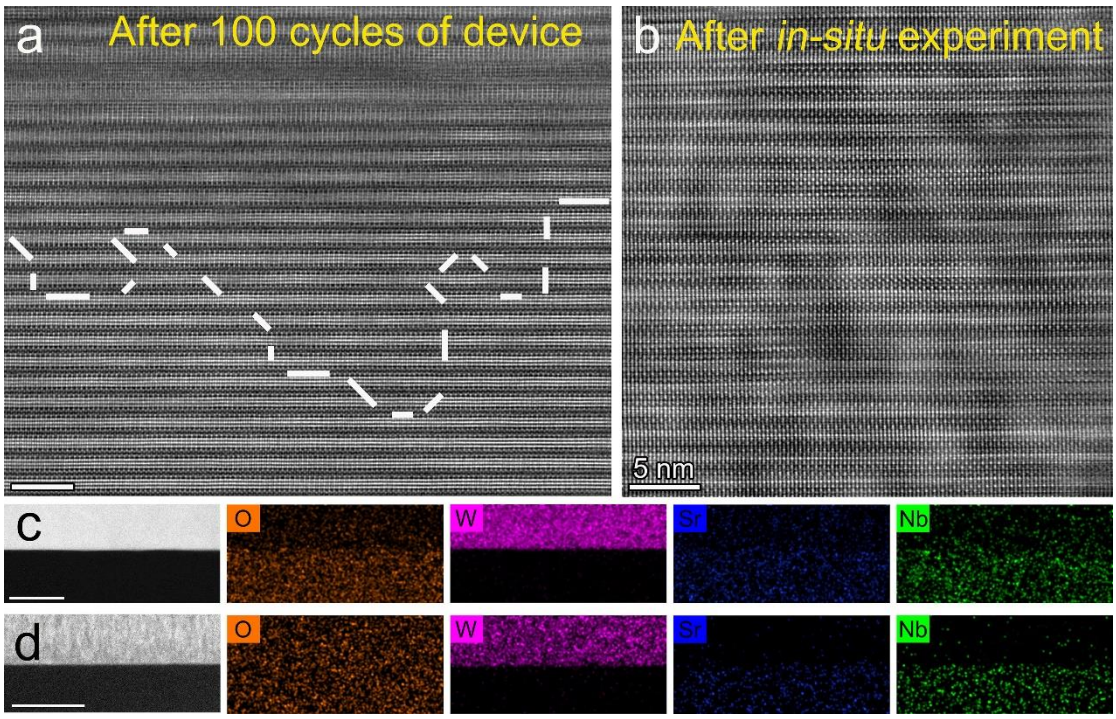

Supplementary Fig. 18. The HAADF images of the W/SNO/NSTO device after 100 cycles. (a, b) The atom-resolved HAADF images after 100 cycles and *in-situ* electrical experiment of the W/SNO/NSTO device. **(c, d)** The cross-sectional EDS elemental mapping of the device before and after cycle. Scale bar = 50 nm.

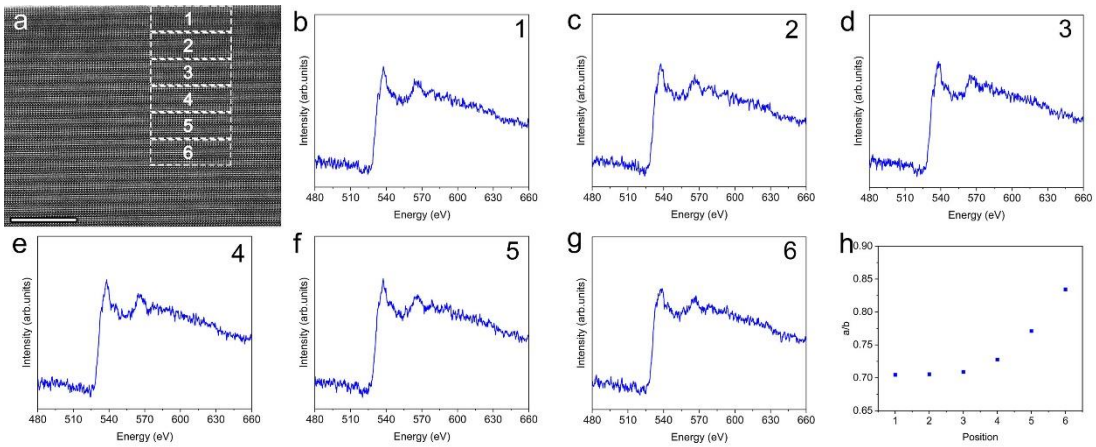

Supplementary Fig. 19. The EELS spectra of the O−K edges after the cycle. (a) The high-resolution HAADF image of SNO. Scale bar=10 nm. **(b-g)** The EELS spectra of the area with dotted white rectangular box in **a**. **(h)** The ratio of EELS peak intensities of oxygen in the 6 regions.

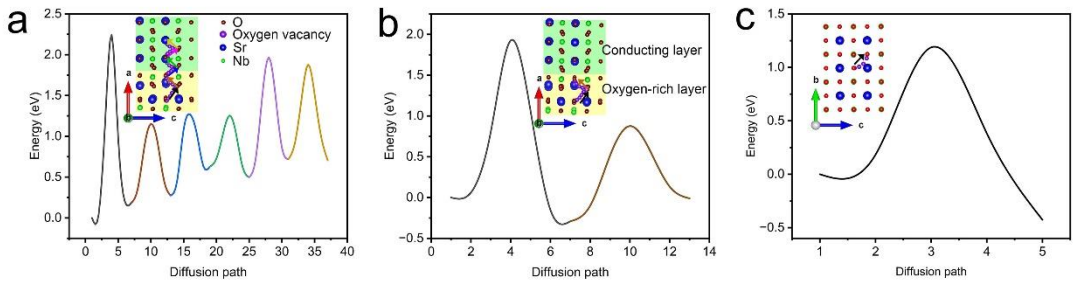

Supplementary Fig. 20. The migration barrier of oxygen vacancy. (a, b) The migration barrier of oxygen vacancy after the appearance of 1 and 3 oxygen vacancies in $SrNbO_{3.4}$. The curve color corresponds to the migration path arrows in the schematic illustration. **(c)** The migration barrier of oxygen vacancy in $SrNbO_3$.

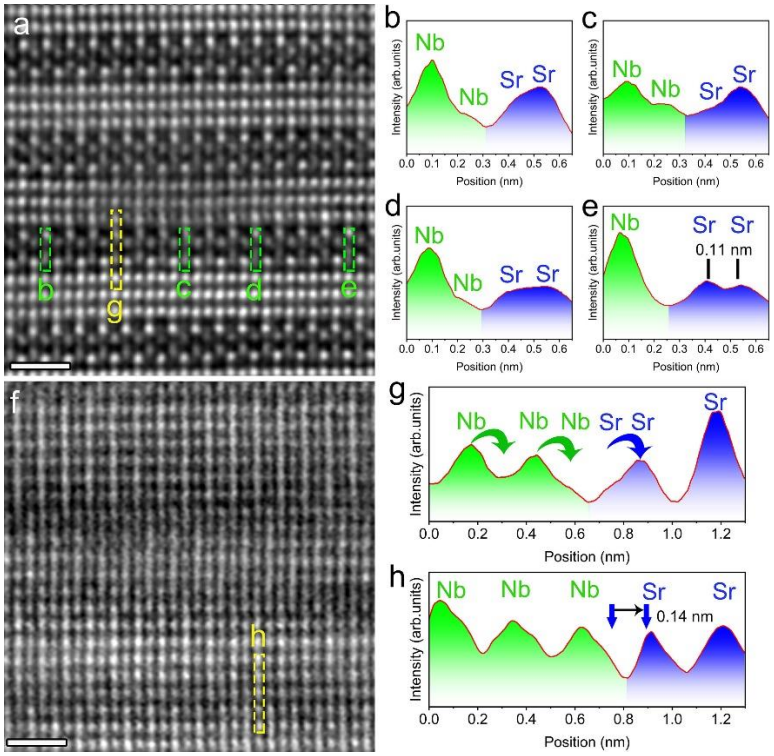

Supplementary Fig. 21. The change of position of Nb atom due to excessive loss of oxygen. (a, f) The atom-resolved HAADF images of the W/SNO/NSTO device after 100 cycles. Scale bar=1 nm. **(b-e, g, h)** The line profiles corresponding to green and yellow rectangular box marked areas in **a, f.**

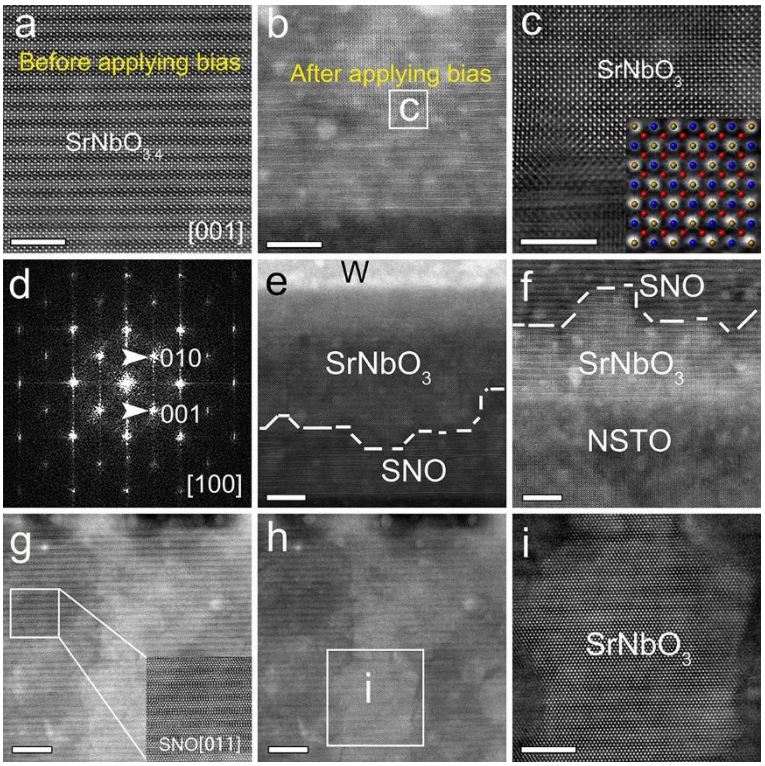

Supplementary Fig. 22. The *in-situ* phase transformation caused by excessive oxygen loss. (a) The HAADF image of the primeval $SrNbO_{3.4}$. Scale bar=5 nm. **(b)** The HAADF image of the $SrNbO_{3.4}$ after applying bias. Scale bar=10 nm. **(c)** The atom-resolved HAADF image of the area with white square frame in **b**. The illustration is an atomic model of $SrNbO_3$ (blue: Sr, green: Nb, red: O). Scale bar=5 nm. **(d)** The FFT image of **c**. **(e, f)** The HAADF images near the upper and lower electrodes. Scale bar=10 nm. **(g-h)** The HAADF image of the $SrNbO_{3.4}$ under different focusing states after applying bias in another *in-situ* experiment. Scale bar=10 nm. **(i)** The atom-resolved HAADF image of the area with white square frame in **h**. Scale bar=5 nm.

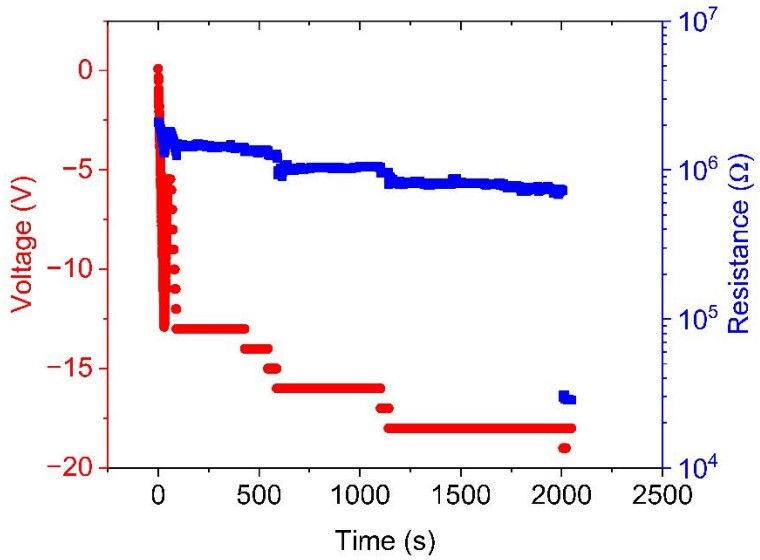

Supplementary Fig. 23. The *in-situ* resistive-voltage characteristics of the W/SNO/NSTO device during bias-induced phase transitions.

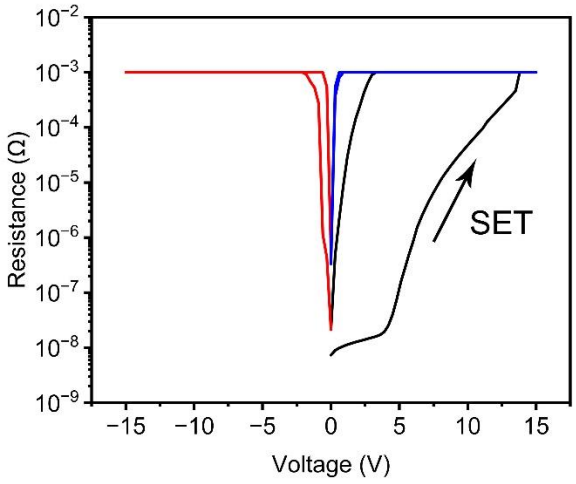

Supplementary Fig. 24. The I–V switching curves of the NSTO/SNO/W device with phase transition during applying bias.

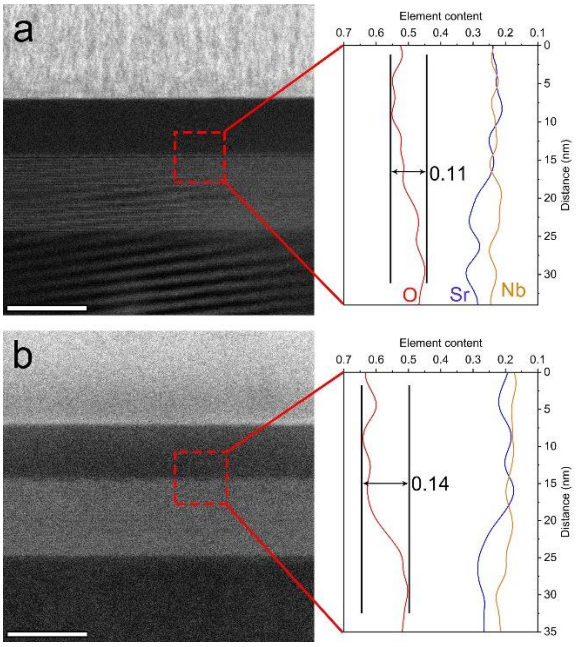

Supplementary Fig. 25. The EDS of oxygen before (a) and after (b) the cycle. Scale bar=50 nm.

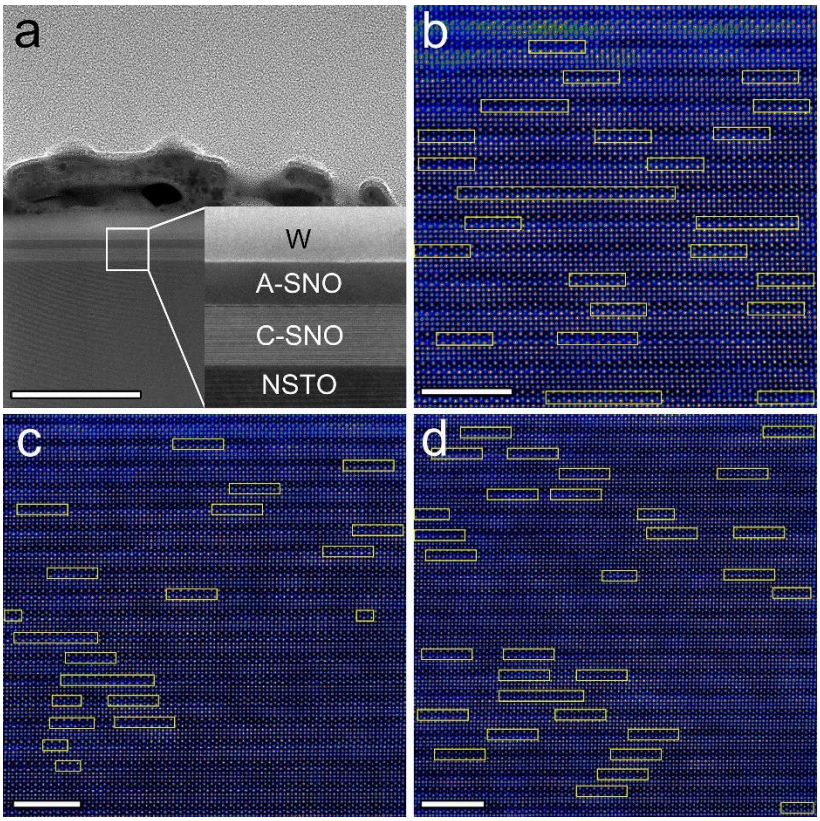

Supplementary Fig. 26. The distribution of oxygen vacancies of the NSTO/C-SNO/A-SNO/W device after 100 cycles. (a) The low power HAADF image at the cross section of the NSTO/C-SNO/A-SNO/W device after cycle. Scale bar=500 nm. **(b-d)** The high resolution HAADF images of C-SNO layer in **a**. Scale bar=5 nm.

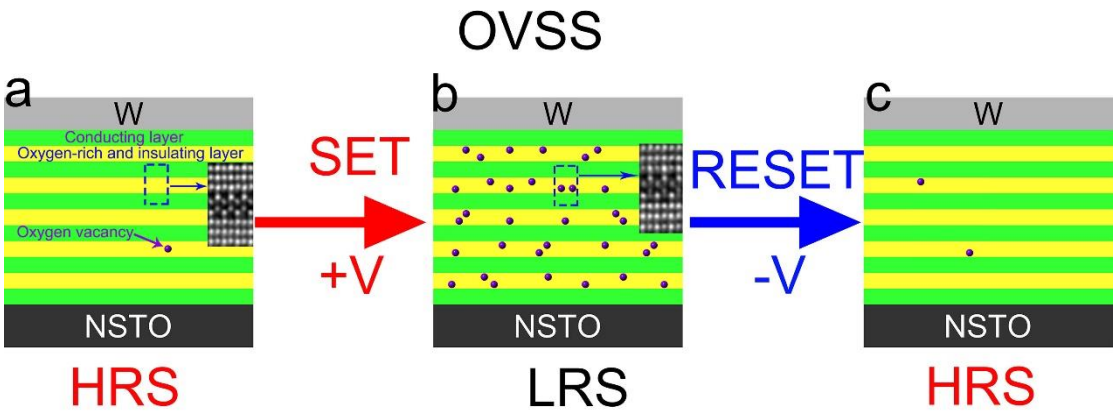

Supplementary Fig. 27. The schematic diagram of the OVSS.

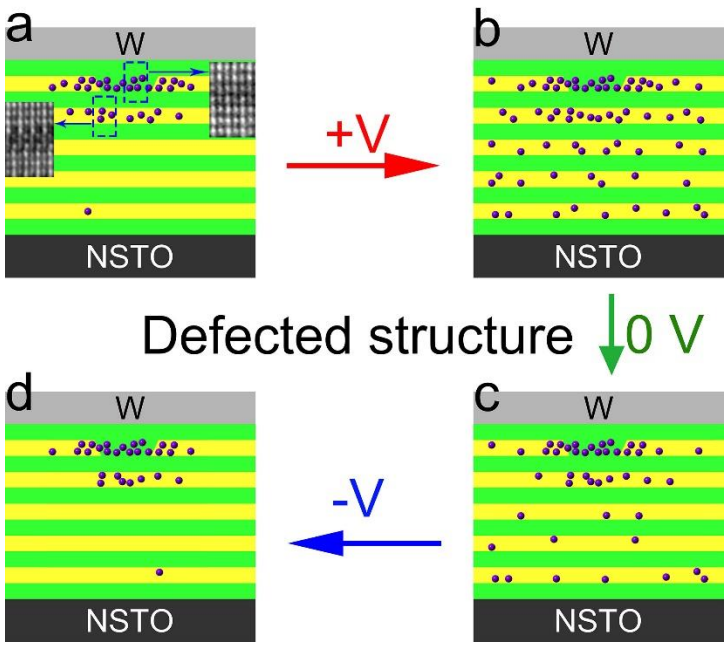

Supplementary Fig. 28. The schematic diagram of the defected structure.

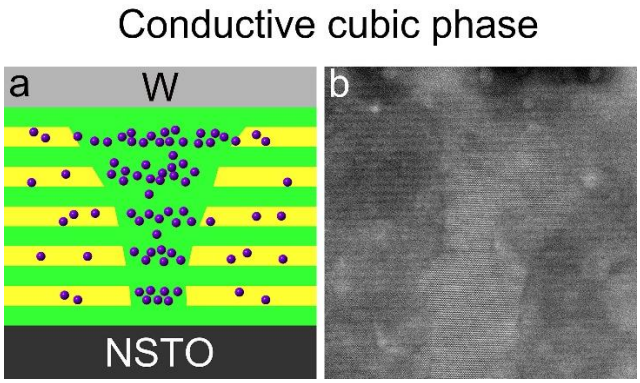

Supplementary Fig. 29. The schematic diagram of the conductive cubic phase.

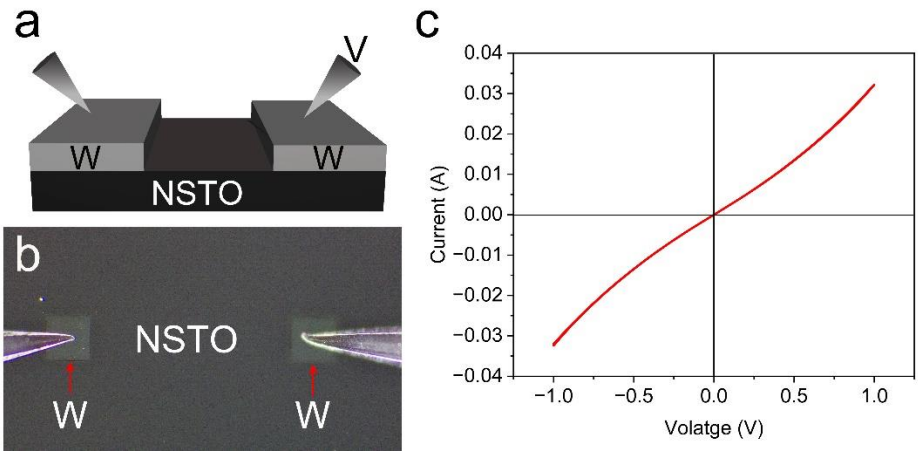

Supplementary Fig. 30. The I-V characteristics of the W/NSTO/W device. (a) The diagram of the W/NSTO/W device. **(b)** The optical microscope image of device. **(c)** The I-V curve of device.

The W/NSTO/W device was prepared to verify whether the substrate NSTO conducts electricity. The results showed that the resistance is ~40 Ω and the device had perfect ohmic contact (Supplementary Fig. 30), indicating that the NSTO is conductive and can be used as the bottom electrode.

Supplementary Table 1. The scanning parameters of the HAADF image.

	Figure 2b	Movie 1
STEM magnification	4.04 Mx	4.04 Mx
Frame time	6.31 s	6.31 s
Screen current	36.3 pA	49.1 pA
Dose rate	1.94×10^4 $e^-/Å^2$	2.62×10^4 $e^-/Å^2$
Frame count	1	47
Total scanning time	6.31 s	296.57 s

Supplementary References

1. Wang M, Cai S, Pan C *et al.* Robust memristors based on layered two-dimensional materials. *Nat. Electron.* 2018; **1**(2): 130-136.
2. Wang X, Yin Y, Song M *et al.* Solution-processable 2D polymer/graphene oxide heterostructure for intrinsic low-current memory device. *ACS Appl. Mater. Interfaces* 2020; **12**(46): 51729-51735.
3. Chen S, Mahmoodi MR, Shi Y *et al.* Wafer-scale integration of two-dimensional materials in high-density memristive crossbar arrays for artificial neural networks. *Nat. Electron.* 2020; **3**(10): 638-645.
4. Ranganathan K, Fiegenbaum-Raz M, Ismach A. Large-scale and robust multifunctional vertically aligned MoS_2 photo-memristors. *Adv. Funct. Mater*. 2020; **30**(51).
5. Li Y, Loh L, Li S *et al.* Anomalous resistive switching in memristors based on two-dimensional palladium diselenide using heterophase grain boundaries. *Nat. Electron*. 2021; **4**(5): 348-356.
6. Ahmed T, Kuriakose S, Tawfik SA *et al.* Mixed ionic-electronic charge transport in layered black-phosphorus for low-power memory. *Adv. Funct. Mater*. 2021; **32**(10).
7. Liu L, Li Y, Huang X *et al.* Low-power memristive logic device enabled by controllable oxidation of 2D $HfSe_2$ for in-memory computing. *Adv. Sci*. 2021; **8**(15).
8. Yin L, Cheng R, Wen Y *et al.* High-performance memristors based on ultrathin 2D copper chalcogenides. *Adv. Mater*. 2022; **34**(9).
9. Yang Y, Du H, Xue Q *et al.* Three-terminal memtransistors based on two-dimensional layered gallium selenide nanosheets for potential low-power electronics applications. *Nano Energ*. 2019; **57**: 566-573.
10. Choi S, Tan SH, Li Z *et al.* SiGe epitaxial memory for neuromorphic computing with reproducible high performance based on engineered dislocations. *Nat. Mater*. 2018; **17**(4): 335-340.
11. Yeon H, Lin P, Choi C *et al.* Alloying conducting channels for reliable neuromorphic computing. *Nat Nanotechnol*. 2020; **15**(7): 574-579.
12. Kim K, Park S, Hu SM *et al.* Enhanced analog synaptic behavior of SiN_x/a-Si bilayer memristors through Ge implantation. *NPG Asia Mater*. 2020; **12**(1).
13. Ilyas N, Li D, Li C *et al.* Analog switching and artificial synaptic behavior of Ag/SiO_x:Ag/TiO_x/p^{++}-Si memristor device. *Nanoscale Res. Lett*. 2020; **15**(1).
14. Li Y, Chu J, Duan W *et al.* Analog and digital bipolar resistive switching in solution-combustion-processed NiO memristor. *ACS Appl. Mater. Interfaces.* 2018; **10**(29): 24598-24606.
15. Sun Y, Xu H, Liu S *et al.* Short-term and long-term plasticity mimicked in low-voltage Ag/GeSe/TiN electronic synapse. *IEEE Electron Device Lett*. 2018; **39**(4): 492-495.
16. Lee T-J, Kim S-K, Seong T-Y. Sputtering-deposited amorphous $SrVO_x$-based memristor for use in neuromorphic computing. *Sci. Rep*. 2020; **10**(1).
17. Boyn S, Grollier J, Lecerf G *et al.* Learning through ferroelectric domain dynamics in solid-state synapses. *Nat. Commun*. 2017; **8**(1).
18. Xing Mou, Jianshi Tang, Yingjie Lyu *et al.* Analog memristive synapse based on topotactic phase transition for high-performance neuromorphic computing and neural network pruning. *Sci. Adv*. 2021; **7**(29): eabh0648.
19. Bessonov AA, Kirikova MN, Petukhov DI *et al.* Layered memristive and memcapacitive switches for printable electronics. *Nat. Mater*. 2014; **14**(2): 199-204.

20. Zhang F, Zhang H, Krylyuk S *et al.* Electric-field induced structural transition in vertical $MoTe_2$- and $Mo_{1-x}W_xTe_2$-based resistive memories. *Nat. Mater*. 2018; **18**(1): 55-61.
21. Wang B, Luo H, Wang X *et al.* Bifunctional NbS_2-based asymmetric heterostructure for lateral and vertical electronic devices. *ACS Nano*. 2019; **14**(1): 175-184.
22. Chen X, Zeng K, Zhu X *et al.* Light driven active transition of switching modes in homogeneous oxides/graphene heterostructure. *Adv. Sci*. 2019; **6**(11).
23. Lee M-J, Lee CB, Lee D *et al.* A fast, high-endurance and scalable non-volatile memory device made from asymmetric Ta_2O_{5-x}/TaO_{2-x} bilayer structures. *Nat. Mater*. 2011; **10**(8): 625-630.
24. Choi BJ, Torrezan AC, Strachan JP *et al.* High-speed and low-energy nitride memristors. *Adv. Funct. Mater*. 2016; **26**(29): 5290-5296.
25. Wang Y, Xu N, Yuan Y *et al.* Achieving adjustable digital-to-analog conversion in memristors with embedded $Cs_2AgSbBr_6$ nanoparticles. *Nanoscale*. 2023; **15**(16): 7344-7351.
26. Zhang Y, Mao G-Q, Zhao X *et al.* Evolution of the conductive filament system in HfO_2-based memristors observed by direct atomic-scale imaging. *Nat. Commun*. 2021; **12**(1).
27. Wu Y, Wei Y, Huang Y *et al.* Capping $CsPbBr_3$ with ZnO to improve performance and stability of perovskite memristors. *Nano Res*. 2016; **10**(5): 1584-1594.